iScience

CellPress
OPEN ACCESS

Article

HDAC1 and HDAC2 orchestrate Wnt signaling to regulate neural progenitor transition during brain development

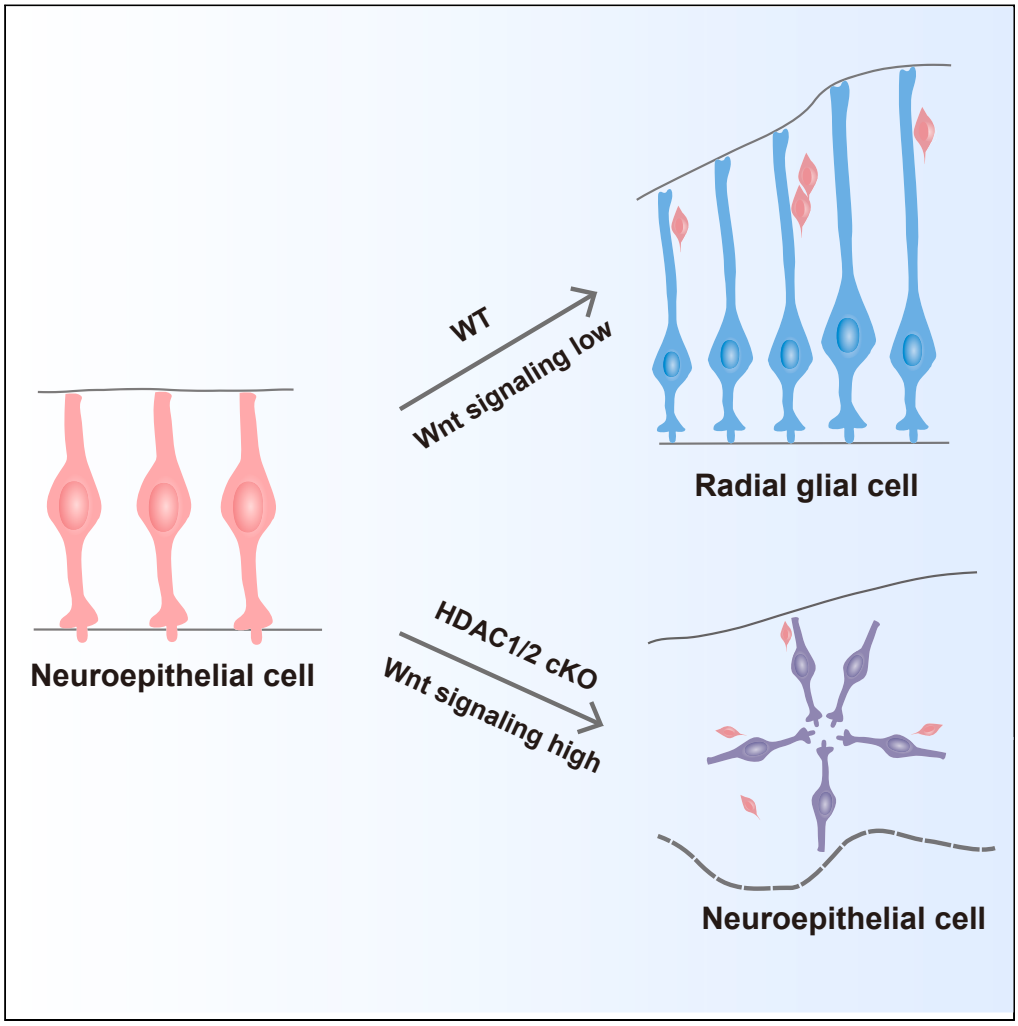

Yue Zhu, Yunyun Huang, Tianxiang Tang, Yunli Xie

yunli.xie@fudan.edu.cn

Highlights

HDAC1/2 promote the transition of neuroepithelial cells to radial glial cells

HDAC1/2 repress Wnt signaling during early cortical neurogenesis

The failure of neuroepithelial transition results in cortical malformation

Low levels of Wnt are essential for neuroepithelial transition

Zhu et al., iScience 27, 110600
September 20, 2024
https://doi.org/10.1016/j.isci.2024.110600

iScience

CellPress
OPEN ACCESS

Article

HDAC1 and HDAC2 orchestrate Wnt signaling to regulate neural progenitor transition during brain development

Yue Zhu,[1,2] Yunyun Huang,[1,2] Tianxiang Tang,[1] and Yunli Xie[1,3,*]

SUMMARY

Tightly controlled neurogenesis is crucial for generating the precise number of neurons and establishing the intricate architecture of the cortex, with deficiencies often leading to neurodevelopmental disorders. Neuroepithelial progenitors (NPs) transit into radial glial progenitors (RGPs) to initiate neural differentiation, yet the governing mechanisms remain elusive. Here, we found that histone deacetylases 1 and 2 (HDAC1/2) mediated suppression of Wnt signaling is essential for the NP-to-RGP transition. Conditional depletion of HDAC1/2 from NPs upregulated Wnt signaling genes, impairing the transition to RGPs and resulting in rosette structures within the neocortex. Multi-omics analysis revealed that HDAC1/2 are critical for downregulating Wnt signaling, identifying Wnt9a as a key target. Overexpression of Wnt9a led to an increased population of NPs and the disruption of cortical organization. Notably, Wnt inhibitor administration partially rescued the disrupted cortical architecture. Our findings reveal the significance of tightly controlled Wnt signaling through epigenetic mechanisms in neocortical development.

INTRODUCTION

Neural progenitors progressively develop into distinct fates to ensure the generation of a precise number of neurons to establish the cortical architecture during brain development. Before the onset of neurogenesis and shortly after the closure of the neural tube, pseudostratified neuroepithelial progenitors (NPs) exhibit bipolar morphology spanning from the apical ventricular to the basal pial surface of the neural tube.[1] These NPs divide symmetrically to expand their number before transiting into radial glial progenitors (RGPs) at the onset of neurogenesis.[2,3] Like NPs, RGPs display apical-basal polarity, with one end anchored to the ventricular surface via an apical process and the other end linked to the pia surface through a basal process. Despite this similarity, RGPs undergo asymmetric divisions to generate either neurons directly or intermediate progenitors (IPs) to produce neurons indirectly.[4] Most, if not all, cortical neurons are differentiated from RGPs during brain development. The transition from NPs to RGCs is essential for the onset of neurogenesis[5] and delayed transition leads to abnormal neurogenesis.[6] However, the underlying mechanisms remain elusive.

The transition from NPs to RGPs is accompanied by changing characteristics in these two distinct population progenitor cells. NPs display typical epithelial features with the presence of tight junctions and adherens junctions at their apical endfeet,[1] With the switch to RGCs, the expression of tight junction protein ZO-1, but not adherens junctions, is reduced.[1] Recent single-cell sequencing analysis reveals that the expression level of numerous genes in NPs and RGPs exhibit distinctions, despite sharing a predominantly similar transcriptome.[7,8] For example, Hmga2 and Zeb2 are highly expressed in NPs and downregulated in RGPs,[8,9] which is consistent with the fact that NPs undergo extensive proliferative divisions while RGPs undergo differentiation progressively. In addition to the difference in transcriptome between these two population progenitors, NPs exhibit distinct morphology which is assumed to be important for their proliferation capacity.[9] The morphological transition to RGPs is also essential for the establishment of neocortical architecture as the apical-basal polarity of RGPs provides the scaffolds for neuronal migration.[10] Therefore, the loss of NP features in RGPs ensures proper neocortical development.

In contrast to neurogenesis stages, the molecular control of the transition from NPs to RGPs remains poorly understood.[11] The transition from NPs to RGPs is regulated by morphogen factors. For example, the transitional expression of Fgf10 is important for the initiation of the transition.[5,6] However, how the extracellular signaling is regulated to control the transition is unclear. Previously we showed that when histone deacetylases 1 and 2 (HDAC1 and HDAC2) were depleted at the early stage of neocortical development, rosette structures within the neocortex were observed,[12] which exhibits a high level of proliferation. Here, we show that these progenitors within the rosette structure exhibit characteristics of NPs and demonstrate that the downregulation of Wnt signaling is essential for the transition of NPs to RGCs, which is controlled by the epigenetic regulators HDAC1 and HDAC2. Depletion of HDAC1 and HDAC2 (referred to as HDAC1/2) led to the increase

[1]Department of Anesthesia, State Key Laboratory of Medical Neurobiology and MOE Frontiers Center for Brain Science, Institutes of Brain Science, and Zhongshan Hospital, Fudan University, Shanghai 200032, China
[2]These authors contributed equally
[3]Lead contact
*Correspondence: yunli.xie@fudan.edu.cn
https://doi.org/10.1016/j.isci.2024.110600

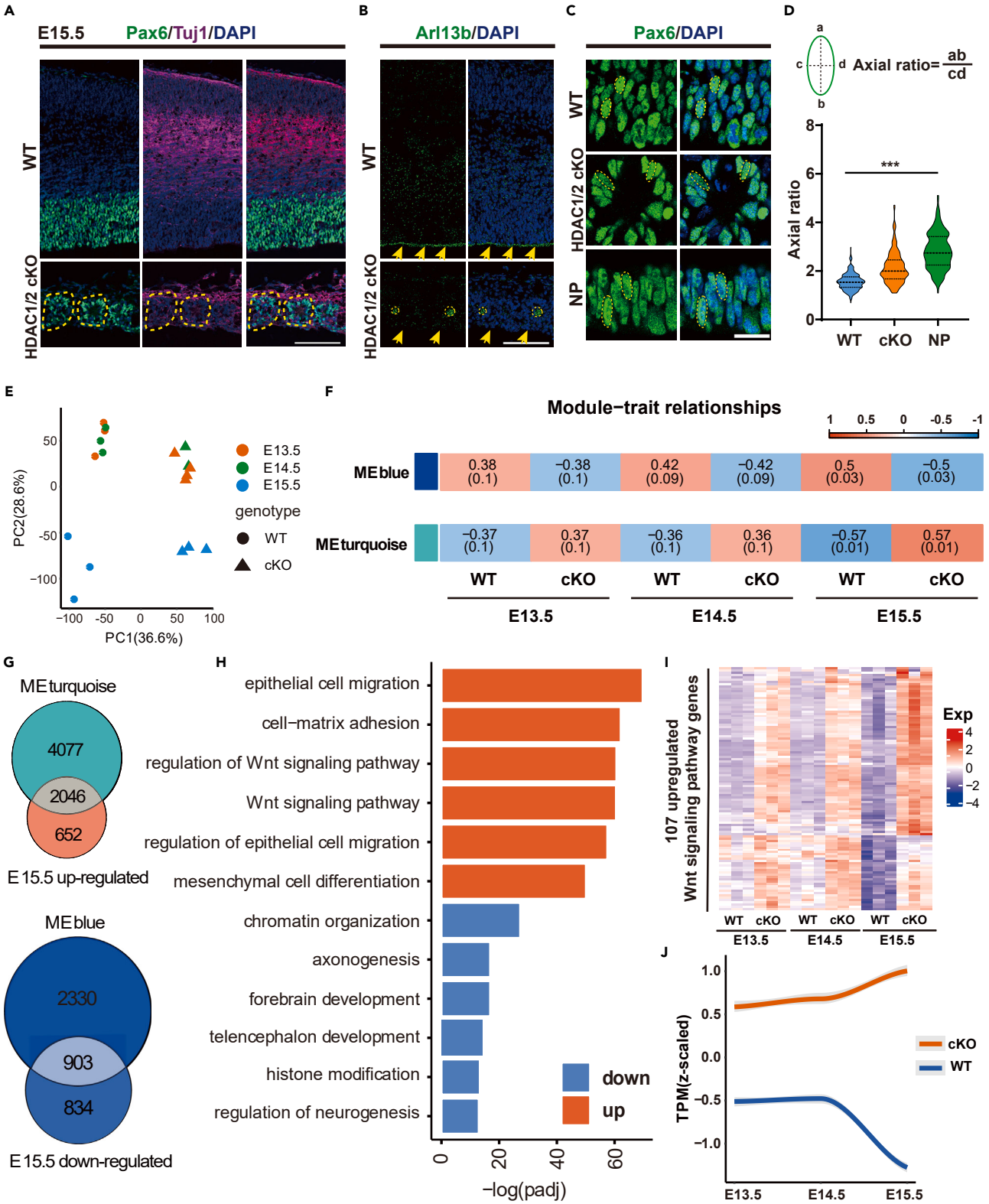
A
E15.5
Pax6/Tuj1/DAPI
WT
HDAC1/2 cKO
B
Arl13b/DAPI
WT
HDAC1/2 cKO
C
Pax6/DAPI
WT
HDAC1/2 cKO
NP
D
a
b
c
d
Axial ratio= ab/cd
Axial ratio
***
WT
cKO
NP
E
PC2(28.6%)
PC1(36.6%)
E13.5
E14.5
E15.5
genotype
WT
cKO
F
Module−trait relationships
1
0.5
0
-0.5
-1
MEblue
0.38 (0.1)
−0.38 (0.1)
0.42 (0.09)
−0.42 (0.09)
0.5 (0.03)
−0.5 (0.03)
MEturquoise
−0.37 (0.1)
0.37 (0.1)
−0.36 (0.1)
0.36 (0.1)
−0.57 (0.01)
0.57 (0.01)
WT
cKO
E13.5
E14.5
E15.5
G
MEturquoise
4077
2046
652
E15.5 up-regulated
MEblue
2330
903
834
E15.5 down-regulated
H
epithelial cell migration
cell−matrix adhesion
regulation of Wnt signaling pathway
Wnt signaling pathway
regulation of epithelial cell migration
mesenchymal cell differentiation
chromatin organization
axonogenesis
forebrain development
telencephalon development
histone modification
regulation of neurogenesis
down
up
−log(padj)
I
107 upregulated Wnt signaling pathway genes
Exp
WT
cKO
E13.5
E14.5
E15.5
J
TPM(z-scaled)
cKO
WT
E13.5
E14.5
E15.5

Figure 1. Depletion of HDAC1/2 leads to an increase of Wnt pathway genes during neocortical development

(A) Immunostaining of the neural progenitor marker Pax6 and neuronal marker Tuj1 in both WT and HDAC1/2 cKO brains at E15.5. Scale bar, 100 μm.

(B) The apical-basal polarity of RGPs was disrupted in HDAC1/2 cKO brains at E15.5. Representative images of Arl13b staining in WT and HDAC1/2 cKO brains are shown. Arrows indicate the ventricular surface. Scale bar, 100 μm.

(C) Images of representative nuclei of E15.5 progenitor cells from WT and HDAC1/2 cKO mice and E9.5 NP cells. Scale bar, 20 μm.

(D) Quantification of the axial ratio (the ratio of its longest axis to its shortest axis) of progenitor cells in E9.5, WT, and HDAC1/2 cKO brains. One-way ANOVA and Tukey's multiple comparisons test was performed. Error bar shows mean ± SEM. ***$p < 0.001$. $n = 3$ brains for each genotype.

(E) PCA plot of E13.5-E15.5 WT and HDAC1/2 cKO bulk RNA-seq sample. $n = 3$ brains for each genotype.

(F) Heatmap depicting the module-trait relationship of the turquoise and blue module. Each cell in the heatmap displays the correlation coefficient between a module eigengene and a trait. The color represents the level of correlation.

(G) The Venn diagram in the upper section depicts the intersection of genes in the turquoise module with genes markedly up-regulated at E15.5 in HDAC1/2 cKO. In the lower section, the Venn diagram elucidates the subset of genes in the blue module that are significantly down-regulated at embryonic day 15.5 in HDAC1/2 cKO.

(H) Gene Ontology enrichment analysis on the overlapping genes identified in (G).

(I) Heatmaps of up-regulated WNT signaling pathway gene expression level (107 genes).

(J) Temporal expression pattern (Z-scaled) of up-regulated WNT signaling pathway genes in WT and HDAC1/2 cKO bulk RNA-seq.

of Wnt effectors, which induced NP-like cells. Furthermore, the prolonged existence of NP-like cells disrupts cortical organization. Therefore, these findings reveal that dynamic expression of the Wnt signaling pathway through epigenetic regulation is essential for the transition to RGPs and thus neocortical development.

RESULTS

Depletion of HDAC1 and HDAC2 leads to an increase of Wnt pathway genes during neocortical development

HDAC1 and HDAC2 are expressed in both NPs and RGPs throughout the neocortical development,[12] with approximately 84% similarity in their amino acid sequences,[13] indicating a significant degree of functional redundancy in multiple biological processes.[14] We did not observe an obvious phenotypic effect on brain development when either HDAC1 or HDAC2 was individually deleted in NPs,[12] further supporting their functional redundancy. For this reason, we depleted both HDAC1 and HDAC2.

Upon the depletion of HDAC1/2 with Emx1Cre-mediated recombination in NPs at embryonic day 10.5 (E10.5), when the transition from NPs to RGPs begins, we found that HDAC1 and HDAC2 were indeed efficiently depleted in NPs (Figure S1). Following the depletion of HDAC1 and HDAC2, we observed that RGPs lost their apical-basal polarity and organized into rosette structures in the neocortex of HDAC1/2 conditional knockout (HDAC1/2 cKO) brains compared with wild type (WT) brains at a later stage (Figures 1A and 1B). These rosette structures are similar to Homer Wright rosettes. Moreover, upon examining the cell nuclei, we found that the progenitor cells within the rosette structure became elongated instead of the round shape observed in the WT brains of the same developmental stage, resembling the nuclear morphology of NP cells at the early E9.5 stage (Figures 1C and 1D). To understand the mechanisms underlying the formation of a rosette structure, we performed transcriptome analysis at E13.5, E14.5, and E15.5, a period covering the development of the rosette structure. Principal component analysis (PCA) revealed a significant difference in transcriptome between WT and HDAC1/2 cKO cortices (Figures 1E and S2A). We found that the transcriptome of early stages (E13.5 and E14.5) was different from that of the late stage (E15.5) in both WT and HDAC1/2 cKO brains (Figure 1E), which is likely due to the increased neuronal production in late stages of brain development.

To investigate whether a consistent gene expression pattern correlates with rosette structure formation during neocortical development, we employed Weighted Gene Co-expression Network Analysis (WGCNA).[15] This approach allowed us to identify 10 co-expressed gene modules (Figure S2B). Notably, within these modules, the turquoise module exhibited continuous upregulation in the HDAC1/2 cKO cortices, while the blue module showed persistent downregulation (Figure 1F). Furthermore, by combing the differential analysis of E15.5 HDAC1/2 cKO and WT samples and employing a Venn diagram, we identified 2046 genes showing an upregulation trend with marked changes at E15.5 and 903 genes displaying a downregulation trend with significant decreases at E15.5 (Figure 1G). Gene Ontology (GO) enrichment analysis revealed that upregulated genes were primarily associated with epithelial cell migration and the Wnt signaling pathway, while the downregulated genes were predominantly enriched in chromatin organization and forebrain development pathways (Figure 1H), suggesting that following the depletion of HDAC1/2, there may be activation of the Wnt signaling pathway and an increase in genes related to epithelial cells. Wnt signaling plays an important role in regulating the proliferation of neural progenitor cells.[16] However, how the Wnt signaling pathway is dynamically regulated during neocortical development remains elusive. Examining the expression of changes in the 107 genes enriched in the Wnt signaling pathway, we observed a gradual decrease in their expression during normal cortical development (Figure 1I). Conversely, in HDAC1/2 cKO cortices, these genes continuously upregulated and became significantly elevated at E15.5 (Figures 1I and 1J). Together, these results demonstrate that HDAC1/2 play a crucial role in regulating the expression level of the Wnt signaling pathway during neocortical development, safeguarding cortical development.

The increase of cortical NPs upon the loss of HDAC1/2

To examine whether the upregulated Wnt signaling pathway genes were expressed by a specific cell subgroup in the HDAC1/2 cKO brains, we leveraged published cortical single-cell transcriptome data for analysis.[8] Employing the singscore algorithm in integrated gene set enrichment

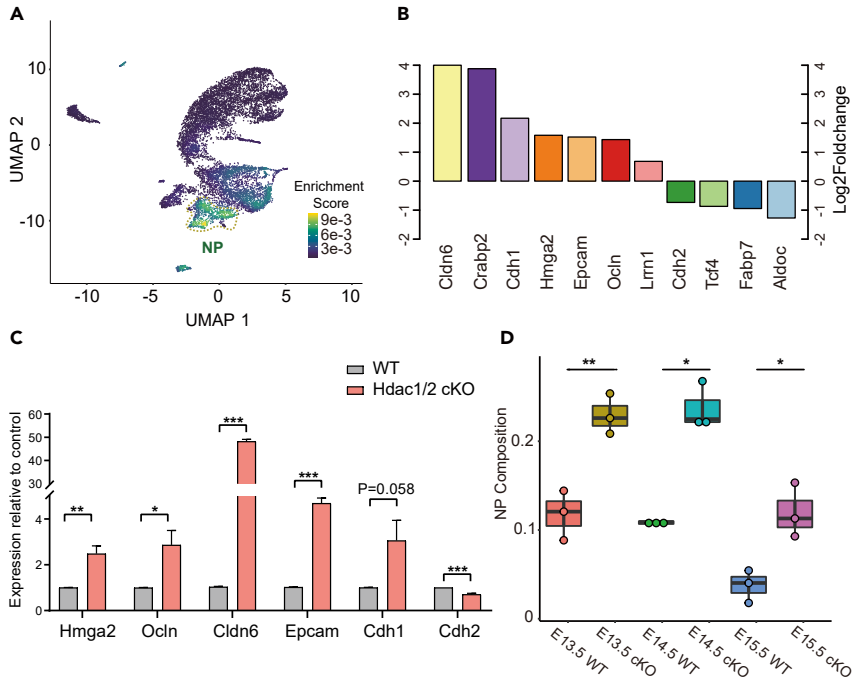

Figure 2. The NP proportion is increased in the HDAC1/2 cKO brain

(A) The density scatterplot shows cell-type enrichment for the 107 up-regulated WNT signaling pathway gene.

(B) Bar plot shows the Log2Foldchange of NP and RGP marker genes in E15.5 derived from bulk RNA-seq differential analysis.

(C) Real-time RT-PCR validation for NP and RGP marker genes. $n = 4$ brains for each genotype. Data are represented as mean ± SEM. Unpaired two-tailed Student's t test was used for statistical analysis, $^{*}p < 0.05$, $^{**}p < 0.01$, $^{***}p < 0.001$. All qRT-PCR data were normalized to the expression of GAPDH.

(D) CIBERSORT cell proportions analysis of E13.5-E15.5 HDAC1/2 cKO brains and WT. NP proportion was higher in HDAC1/2 cKO brains. Mean ± SEM. $n = 3$ brains for each genotype. Unpaired two-tailed Student's t test, $^{*}p < 0.05$, $^{**}p < 0.01$.

analysis (irGSEA),[17] we analyzed gene enrichment scores for cell type specificity. Notably, we found a significant enrichment of the set of Wnt signaling pathway genes in the NPs group (Figures 2A and S3A).

The transition from NPs to RGPs occurs at the onset of neurogenesis. To investigate whether NPs failed to transform into RGPs following HDAC1/2 depletion, we examined the expression of NP marker genes at the E15.5 when rosette structures exist in the neocortex (Figure 1A).[12] We found a significant enrichment of NP marker genes in HDAC1/2 cKO brains, including Clnd6, Crabp2, E-cadherin, and Epcam (Figure 2B). In contrast, the expression levels of RGP marker genes such as Aldoc, Fabp7, and Cdh2 were downregulated (Figure 2B). Furthermore, quantitative PCR (qPCR) results concurred with RNA-seq findings, demonstrating a significant increase in the expression of NP cell markers in progenitors of HDAC1/2 cKO cortices (Figure 2C). To validate these findings on a broader scale, we employed the cell deconvolution algorithm in CIBERSORT[18] to calculate the proportion of NPs in bulk RNA-seq data. Consistently, we observed a higher proportion of NPs in the HDAC1/2 cKO brain, while the opposite trend was noted for RGPs (Figures 2D and S3B). Taken together, these results indicate that NPs failed to undergo a transition into RGPs following HDAC1/2 depletion during cortical development.

Single-cell analysis reveals defects in the transition from NPs to RGPs

To further investigate how the transition from NPs to RGPs was disrupted upon the loss of HDAC1/2, we conducted single-cell RNA sequencing (scRNA-seq) analysis on the cortices of HDAC1/2 cKO and WT mice at an early stage E12.5. Following quality control and removal of low-quality cells, a total of 29,281 cells were obtained, with 14,213 cells in the WT samples and 15,068 cells in HDAC1/2 cKO samples. The unsupervised Louvain clustering algorithm identified 11 cell clusters, including progenitor cells, intermediate progenitor cells (IPCs), neurons, Cajal-Retzius cells (CRs), interneurons, vascular leptomeningeal cells, endothelial cells, and microglia (Figures S4A–S4C). For focused analysis on the dorsal cortical progenitor lineage, interneurons, non-neuronal cells, and progenitor cells of the ventral neocortex were excluded. Clustering and dimensionality reduction analyses on the remaining cells revealed the distinct neural progenitor cell (progenitor)-IPC-Neuron lineage in the UMAP plot (Figure 3A). Interestingly, despite expressing neural progenitor cell markers like Hes5 and Id4, progenitors from the HDAC1/2 cKO and WT groups failed to cluster together, unlike IPCs and neurons (Figures 3A–3C), indicating significant transcriptomic changes in early progenitors following HDAC1/2 knockout.

To determine whether progenitor cells in the HDAC1/2 cKO cortex exhibited NP features, we analyzed published cortical scRNA-seq data from E10.5 and E12.5, which distinctly show NP and RGP populations.[19] Using Pearson correlation, we found that, at the transcriptome level, progenitor cells in the HDAC1/2 cKO brain were similar to E10.5 NPs (Figure 3D). Dimensionality reduction and clustering of merged cells

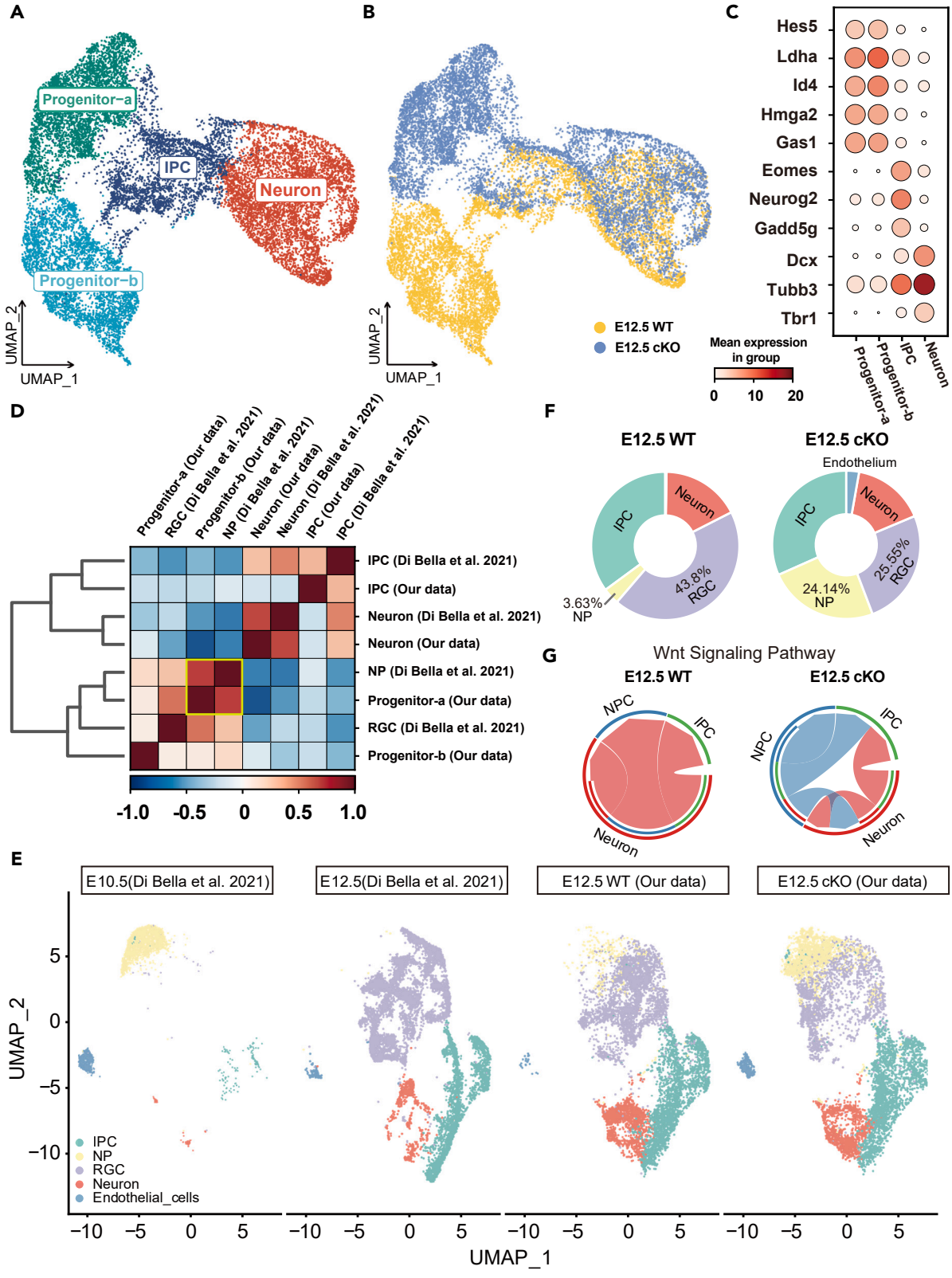
A
Progenitor−a
IPC
Neuron
Progenitor−b
UMAP_2
UMAP_1
B
UMAP_2
UMAP_1
E12.5 WT
E12.5 cKO
C
Hes5
Ldha
Id4
Hmga2
Gas1
Eomes
Neurog2
Gadd5g
Dcx
Tubb3
Tbr1
Mean expression in group
0
10
20
Progenitor-a
Progenitor-b
IPC
Neuron
D
Progenitor-a (Our data)
RGC (Di Bella et al. 2021)
Progenitor-b (Our data)
NP (Di Bella et al. 2021)
Neuron (Our data)
Neuron (Di Bella et al. 2021)
IPC (Our data)
IPC (Di Bella et al. 2021)
IPC (Di Bella et al. 2021)
IPC (Our data)
Neuron (Di Bella et al. 2021)
Neuron (Our data)
NP (Di Bella et al. 2021)
Progenitor-a (Our data)
RGC (Di Bella et al. 2021)
Progenitor-b (Our data)
-1.0
-0.5
0
0.5
1.0
F
E12.5 WT
E12.5 cKO
Endothelium
IPC
Neuron
43.8% RGC
3.63% NP
24.14% NP
25.55% RGC
G
Wnt Signaling Pathway
E12.5 WT
E12.5 cKO
NPC
IPC
Neuron
E
E10.5(Di Bella et al. 2021)
E12.5(Di Bella et al. 2021)
E12.5 WT (Our data)
E12.5 cKO (Our data)
UMAP_2
UMAP_1
IPC
NP
RGC
Neuron
Endothelial_cells

Figure 3. Single-cell analysis reveals deficiencies in the transition from NPs to RGPs upon the loss of HDAC1/2

(A and B) UMAP visualization of E12.5 cortical cells from HDAC1/2 cKO and WT brain group by cell type (A) and genotype type (B).

(C) Dot plot depicting the relative gene expression and the distribution of marker genes across different cell clusters. The size of each dot indicates the percentage of the gene corresponding to a specific cell cluster, while the color gradient shows the mean of normalized gene expression categorized by cluster.

(D) Pearson's correlation coefficient analysis compares each cell cluster from our dataset with those reported in Di Bella et al., 2021.

(E) UMAP visualization of E12.5 cells from HDAC1/2 and WT cortices and E10, E12.5 cells from Di Bella et al. 2021.

(F) Doughnut plot illustrating the composition and respective proportions of all cell types within the HDAC1/2 cKO and WT brains.

(G) Chord diagram showing the interactions between different cell groups through the Wnt signaling pathway network. The inner thinner bar colors represent the targets that receive signal from the corresponding outer bar. The inner bar size is proportional to the signal strength received by the targets.

further demonstrated that the number of NPs was significantly increased in HDAC1/2 cKO compared to WT brains (Figures 3E, 3F, and S4D). Furthermore, CellChat[20] analysis analyzing cell-cell communication, showed that NPs in the HDAC1/2 cKO brain exhibited increased secretion and reception of Wnt signals (Figure 3G), indicating the potential activation of the Wnt signaling pathway in these cells. Together, these results indicate that progenitor cells in the HDAC1/2 cKO brain adopt the characteristics of NPs.

HDAC1/2 exert repressive control on the Wnt signaling pathway

HDAC1/2 remove acetyl groups from histone tails to modulate chromatin states and regulate gene expression.[21] To understand how HDAC1/2 regulate the Wnt signaling pathway, we performed H3K27ac Cleavage Under Targets & Tagmentation (CUT&Tag) experiments[22] on dorsal neocortex following HDAC1/2 depletion (Figure 4A). Principal component analysis (PCA) revealed significant differences between the WT and HDAC1/2 cKO samples on PC1 (Figure 4B). Differential analysis using DiffBind showed that the majority of peaks exhibited increased levels of H3K27 acetylation after HDAC1/2 knockout, with a minority showing a decrease (Figure 4C). Annotation of the peaks with increased H3K27ac indicated a predominant presence in the promoter regions of genes (Figure 4D). Given the importance of H3K27ac enrichment in proximity to the transcription start site (TSS) for activating genes, a Gene Ontology (GO) analysis of H3K27ac peaks associated genes revealed an enrichment of the Wnt signaling pathway (Figure 4E), suggesting that HDAC1/2 may regulate the expression of Wnt signaling pathway genes. As a member of the Sin3, NuRD, and CoREST co-repressor complex, HDAC1/2 is often recruited by transcription factors to exert its function.[13] Homer motif analysis[23] of peaks with increased H3K27ac suggested potential binding by transcription factors such as Zeb2 (Figure 4F), known for promoting epithelial-to-mesenchymal transition (EMT)[24] and playing a role in the transition from NP cells to RGPs transition during human brain development,[9] implying that HDAC1/2 may collaborate with Zeb2 to facilitate the NP-to-RGP transition. Additionally, the annotation of peaks with decreased H3K27ac levels revealed that nearly half of the downregulated peaks were situated in the promoter regions of genes (Figures S5A and S5D). GO enrichment analysis of these genes showed that they were primarily associated with neuronal development (Figure S5B). This aligns with observations of reduced neurogenesis and thinning of the cerebral cortex after HDAC1/2 knockout. Motif analysis of peaks with decreased H3K27ac modification suggested potential binding by transcription factors such as Gfi1b, SF1, and Nanog (Figure S5C). Therefore, these results suggest that HDAC1/2 control the Wnt signaling pathway through epigenetic regulation. To further refine the potential targets of HDAC1/2, we integrated data from upregulated Wnt genes identified by bulk RNA-seq, upregulated Wnt genes with increased H3K27ac signal, and published HDAC1/2 ChIP-seq data[25] (Figure 4G). Noteworthy, amongst the Wnt ligands, the expression of Wnt9a, Wnt5b, Wnt5a, and Wnt2b was increased following HDAC1/2 knockout, featuring HDAC1/2 binding in their gene promoter regions and elevated H3K27ac levels in these regions (Figures 4G and 4H). Taken together, these results demonstrate that HDAC1/2 repress the expression of the Wnt signaling pathway genes during neocortical development.

Overexpression of Wnt9a and Wnt5b in RGPs leads to the formation of rosette structures in the neocortex

In the HDAC1/2 cKO cortex, the sustained expression of the Wnt signaling pathway genes hindered the transition of NPs into RGPs, ultimately leading to the formation of a rosette structure. Among the upregulated Wnt ligands, Wnt9a and Wnt5b exhibited the most significant changes in expression upon the loss of HDAC1/2 (Figure 4G). To ask whether the overexpression of Wnt9a or Wnt5b in RGPs alters their fate, we performed *in utero* electroporation (IUE) with plasmids expressing either Wnt9a or Wn5b in RGPs at E12.5 (Figures 5 and S6). Shortly after the electroporation (24 h later), it became apparent that the overexpression of Wnt9a rapidly induced abnormal distribution of progenitor cells and rosette-like structure formation (Figure 5A), mirroring the phenotype observed following HDAC1/2 depletion.[12] Prolonged expression of Wnt9a further induced abnormal distribution of Pax6+ progenitor cells (Figure 5B). To further assess whether the apical-basal polarity of the progenitor cells was affected, we stained the sections with tight junction marker zona occludens-1 (ZO-1) and the cilia marker Arl13b and found that overexpression of Wnt9a disrupted the tight junction at the apical surface of the ventricular (Figure 5C). In addition, clustered cilia were observed within the rosette structures (Figure 5C). Rosette structures were present in 4 out of 5 brain samples (80%) following Wnt9a overexpression. Similarly, Wnt5b overexpression induced rosette formation and led to a disorganized cortical structure (Figures S6A–S6C), with rosette structures observed in 2 out of 3 brain samples (66.6%). These results demonstrate that the downregulation of the Wnt signaling pathway is essential to safeguard the organization of progenitor cells during cortical development.

Wnt9a-induced progenitor cells exhibit NP cell features

To further examine whether the progenitor cells induced by the overexpression of Wnt9a have NP characteristics, we performed transcriptome analysis on cortices following Wnt9a overexpression (Figure 6A). PCA analysis revealed that PC1 was predominantly associated with

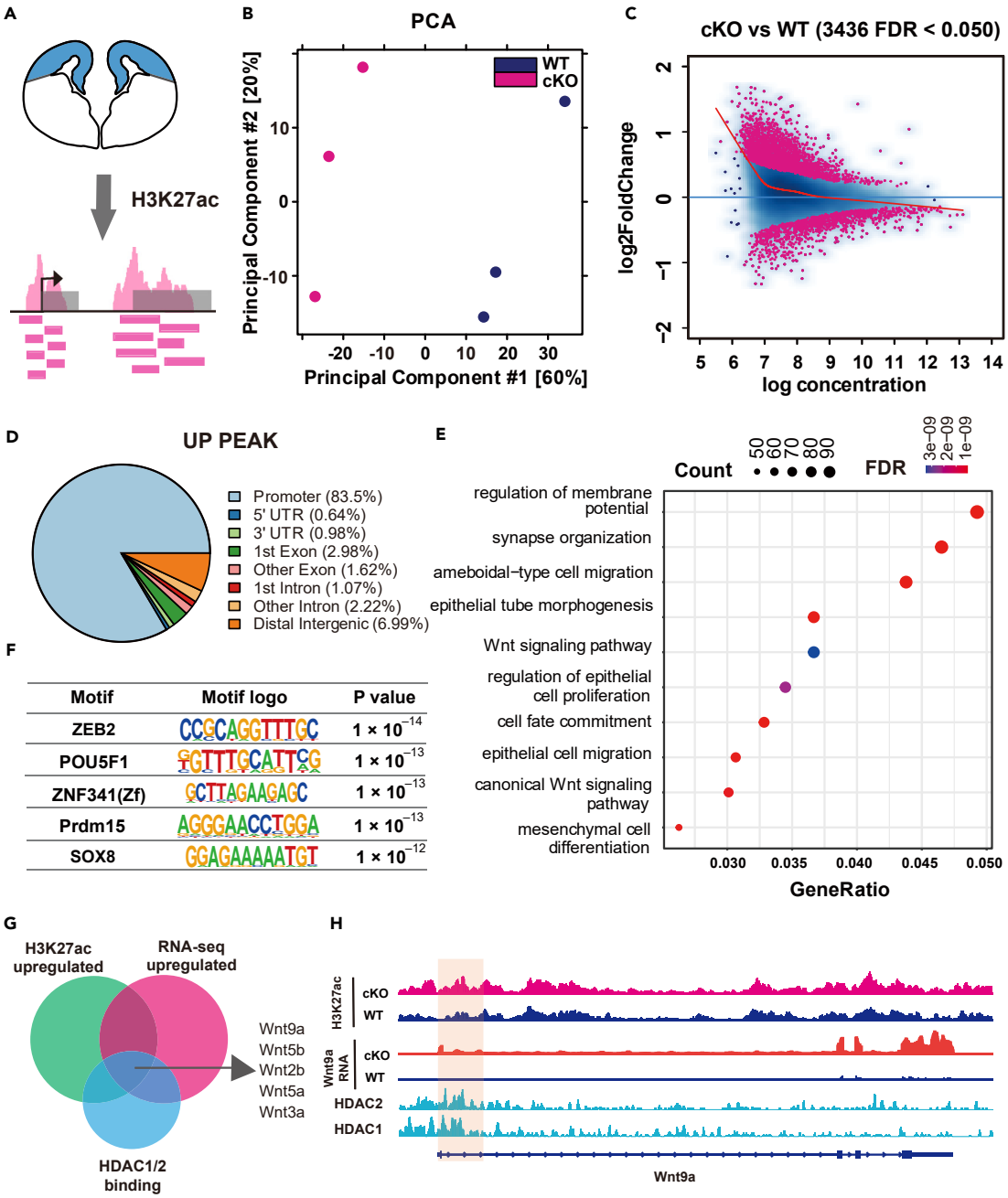

Figure 4. HDAC1/2 repress the expression of Wnt signaling pathway genes

(A) Schematic representation of the experimental approach.

(B) PCA plot of H3K27ac CUT&Tag from HDAC1/2 cKO and WT brains.

(C) MA plot of differential (HDAC1/2 cKO/WT) H3K27ac CUT&Tag peaks. Peaks identified as exhibiting significant differential binding are highlighted in red.

(D) Genome annotations for up-regulated H3K27ac CUT&Tag peaks.

(E) Gene Ontology enrichment analysis for genes associated with up-regulated H3K27ac peaks.

(F) Top Motifs enriched in up-regulated H3K27ac peaks by HOMER (cumulative binomial distributions).

(G) The intersection of H3K27ac up-regulated, RNA-seq up-regulated, and HDAC1/2 binding Wnt ligand genes.

(H) Integrative Genomics Viewer (IGV) map tracks displaying RNA-seq, H3K27ac CUT&Tag signals, and HDAC1/2 signals at the Wnt9a loci.

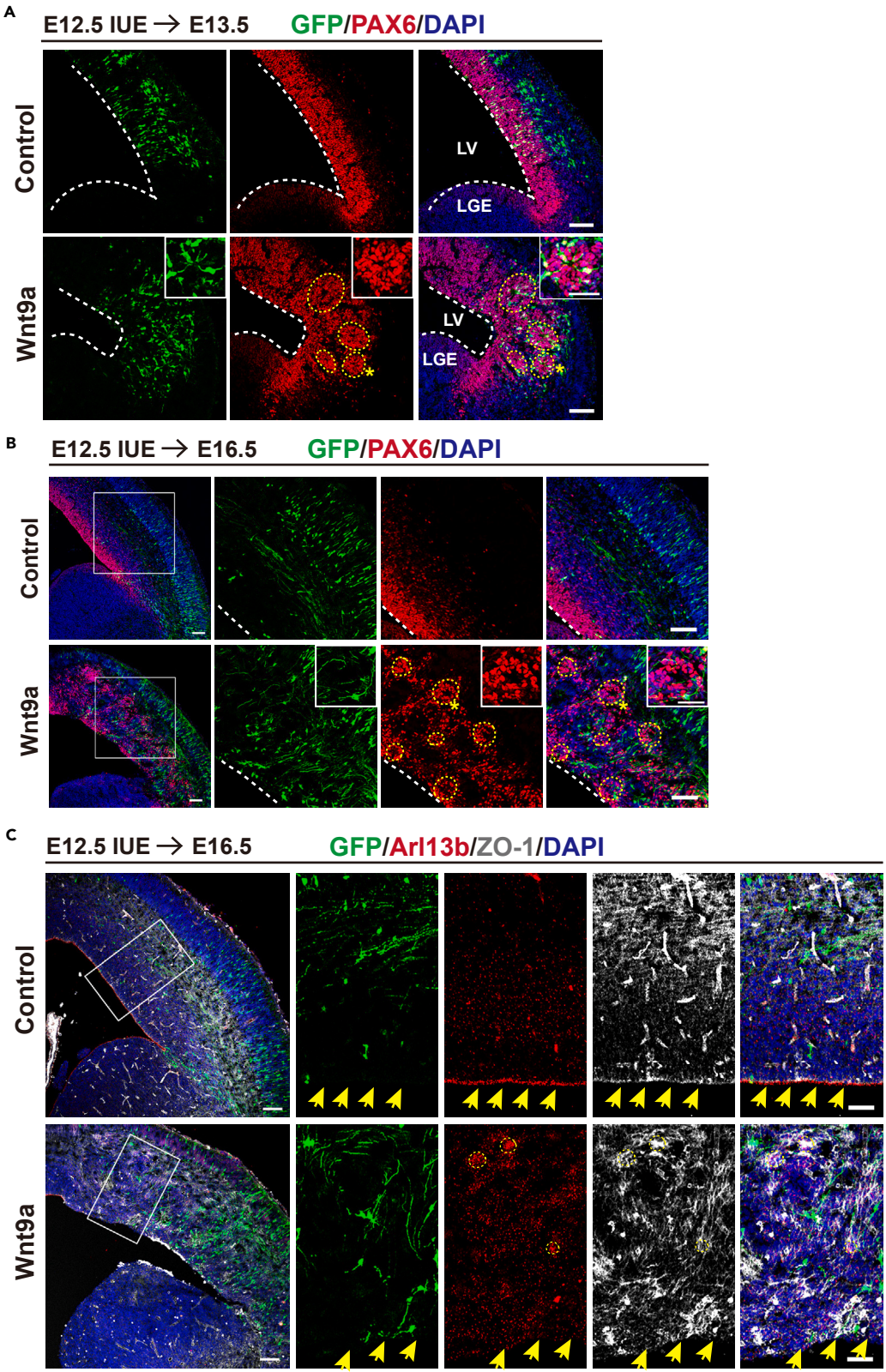
A
E12.5 IUE → E13.5
GFP/PAX6/DAPI
Control
Wnt9a
LV
LGE
LV
LGE
B
E12.5 IUE → E16.5
GFP/PAX6/DAPI
Control
Wnt9a
C
E12.5 IUE → E16.5
GFP/Arl13b/ZO-1/DAPI
Control
Wnt9a

Figure 5. Overexpression of Wnt9a in RGPs leads to the formation of rosette structures

(A) Overexpression of Wnt9a in progenitor cells induced abnormal distribution of progenitor cells. Images of sections stained for Pax6 or GFP from brains electroporated with plasmids expressing GFP or Wnt9a. At least three brains were analyzed. The square highlights one rosette structure, shown in detail. Scale bars represent 100 μm for the main image and 50 μm for the inset.

(B) Images of sections stained for Pax6 or GFP. At least three brains were analyzed for each genotype. Scale bar, 100 μm. The square highlights one rosette structure, shown in detail. Scale bars represent 100 μm for the main image and 50 μm for the inset.

(C) Overexpression of Wnt9a in progenitor cells disrupted the apical-basal polarity. Images of sections stained for Arl13b and ZO-1. At least three brains were analyzed. Scale bar: 50 μm.

Wnt9a overexpression, explaining 72% of the variance (Figure S7A). The overexpression of Wnt9a led to a notable upregulation in the expression of the majority of genes, with a subset showing reduced expression (Figure 6B). Notably, the upregulated genes were enriched in not only the Wnt signaling pathway but also extracellular matrix organization and epithelial tube morphogenesis (Figure S7B), aligning with pathways enriched in upregulated genes after HDAC1/2 cKO (Figure 1F). Conversely, the downregulated genes were enriched in processes related to the regulation of neural development (Figure S7C). Furthermore, the majority of the upregulated genes in Wnt9a overexpression coincided with these upregulated in HDAC1/2 cKO. These shared genes were enriched in the same pathways as observed in HDAC1/2 cKO (Figures 6C and 6D), suggesting that the formation of the rosette structure, observed upon the loss of HDAC1/2, is induced by the upregulation of the Wnt signaling pathway. Notably, the analysis of gene expression in the Wnt9a overexpression samples demonstrated a significant upregulation of NP marker genes, including Cdh1, Epcam, Cldn6, and Hmga2 (Figure 6E). Subsequently, cell type enrichment analysis on the overlapped 622 genes revealed that these genes were primarily expressed in cells annotated as NPs (Figure 6F). Taken together, these data demonstrate that upregulation of the Wnt signaling pathway, exemplified by Wnt9a, induces NP features.

We then investigated whether inhibiting the Wnt signaling pathway could attenuate the abnormalities in progenitor organization resulting from the depletion of HDAC1/2. To address this, we administrated the Wnt inhibitor XAV-939[26] into the brain ventricle at E12.5, which was analyzed at E15.5 (Figure S8A). By examining the progenitor marker Pax6 and the adherens junction marker N-cadherin, the Wnt inhibitor restored the apical-basal polarity of progenitors and prevented the formation of rosette structures (Figure S8B). Taken together, our findings indicate that the downregulation of the Wnt signaling pathway is essential for regulating NP-to-RGP transition and the cortical organization of progenitors.

DISCUSSION

Tight controlled progenitor transition safeguards neuronal production and the integrity of the cortical architecture during brain development. To generate a proper number of neurons, NPs need to transition into RGPs timely at the onset of neurogenesis. This study demonstrated that downregulation of the Wnt signaling pathway is essential for RGPs to lose NP features and promotes the transition from NPs to RGPs during cortical development. This process is controlled by HDAC1/2-mediated epigenetic regulation. Persistent expression of the Wnt signal pathway genes causes the failure in the transition from NPs to RGPs and ultimately disrupts the cortical architecture (Figure 6G). Thus, our data reveal an essential role for the dynamic activation of the Wnt signaling pathway during neocortical development.

NPs within the neuroepithelium are the founder cells for neural progenitors[27] and exhibit unique features with distinct morphology, which is believed to be important for cortical expansion.[9] NPs express a high level of tight junction components with typical epithelial features.[28] However, upon the onset of neurogenesis, RGPs lose certain epithelial features, particularly tight junctions (but not adherens junctions).[1] Therefore, the transition from the NP cells to RGPs is essential for the generation of neurons during cortical development. Consistently, we found that progenitors within the rosette structure in HDAC1/2 cKO brains express multiple genes related to NPs (Figure 6) and fail to generate superficial layer neurons at late stages of cortical development,[12] highlighting the importance of the loss of NP features in RGPs. Notably, RGPs have distinct morphology compared to NPs.[1,9] The morphological transition enables differentiated neurons to migrate to the cortical plate along the basal processes of RGPs.[29] Overexpression of Wnt9a induces NP cell-like features in RGPs, which reorganizes progenitor cells into rosette structures. Therefore, the transition from NP cells to RGPs not only ensures proper neuronal production but also safeguards cortical architecture during brain development. Rosette formation emerges as a crucial factor in the context of brain tumors,[30,31] underscoring the potential therapeutic strategies. Wnt signaling is essential for the maintenance of neural progenitor proliferation.[16,32] However, how the Wnt signaling regulates NP transition remains unclear. Activation of the Wnt signaling pathway by the overexpression of beta-catenin leads to progenitor over-proliferation,[16] reminiscent of the increased progenitor proliferation within the rosette structures and the thinner cortex in HDAC1/2 cKO brains. Although the detailed cell identity was not clarified upon the activation of beta-catenin, these progenitors are likely different from RGCs. Altogether, downregulation of the Wnt signaling is essential for the transition from NPs to RGCs upon the onset of neurogenesis. Here, we uncover that the dynamic expression of genes related to the Wnt signaling is regulated by the epigenetic factors HDAC1/2, which safeguards cortical development. The progenitor diversity in the human brain is more complicated and proper progression of these progenitors is essential for brain development, therefore, it would be interesting to investigate how the Wnt signaling is regulated during human brain development in the future.

Limitations of the study

In this study, we observed an interesting phenomenon: neural stem cells form a rosette structure when the Wnt signaling pathway is activated. However, it is worth noting that in *in-vitro* culture system experiments, cells can autonomously form this rosette structure even without the

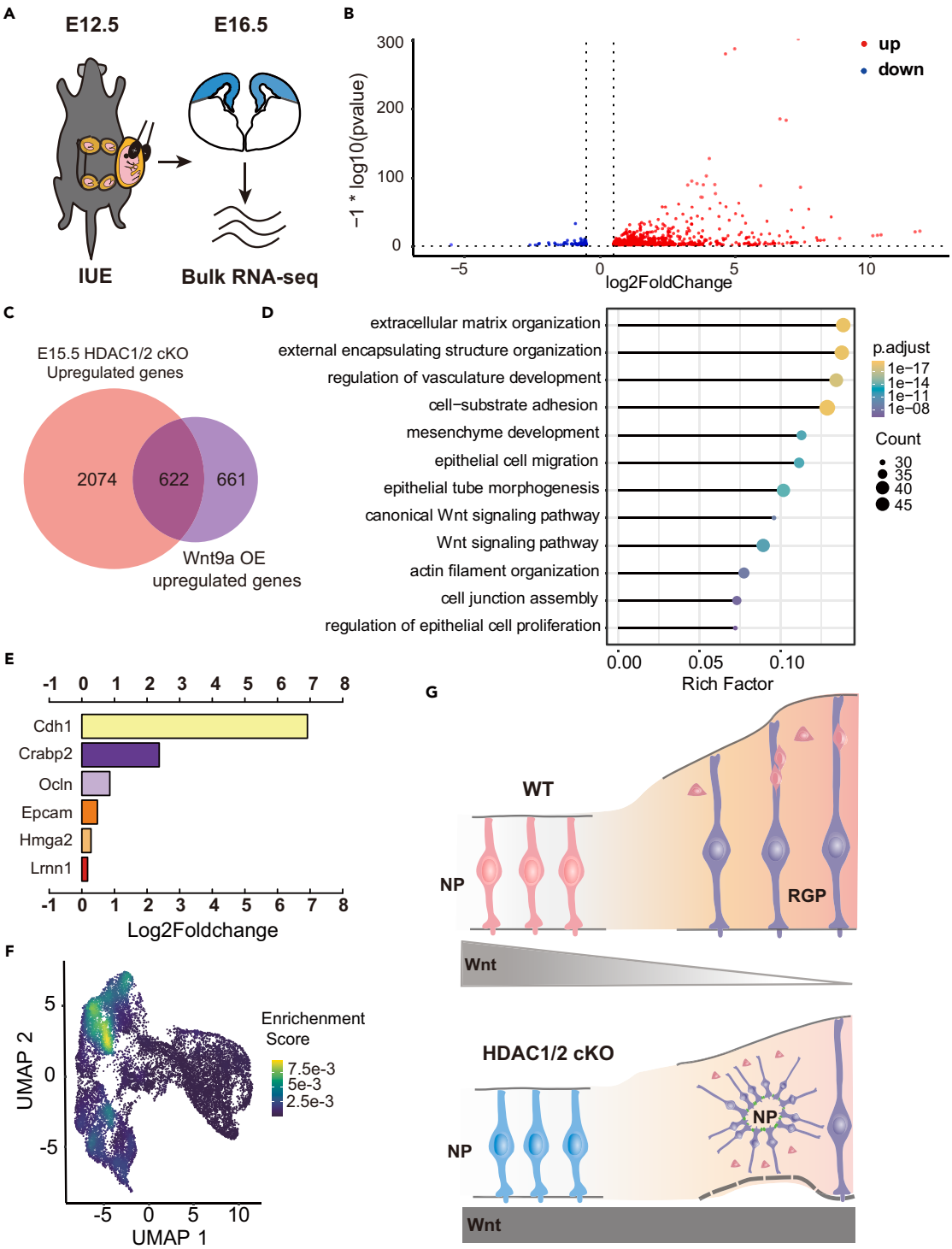

Figure 6. Wnt9a-induced progenitor cells exhibit NP features

(A) Schematic representation of the Bulk RNA-seq process.

(B) Volcano plot of the comparison between Wnt9a overexpression (OE) and control brains. Genes exhibiting significant differential expression are highlighted: up-regulated in red and down-regulated in blue. The significance threshold is set at an absolute Log2Foldchange greater than 0.5 and an adjusted *p*-value (padj) of 0.05 or less.

(C) Venn diagrams illustrate the overlap between genes up-regulated by Wnt9a overexpression (OE) and genes significantly up-regulated in E15.5 HDAC1/2 cKO models.

Figure 6. *Continued*

(D) Gene Ontology enrichment analysis was conducted on the overlapping genes identified in (C).

(E) Bar plot shows Log2Foldchange of NP marker genes derived from bulk RNA-seq differential analysis comparing Wnt9a OE brain to control.

(F) Density scatterplot shows cell-type enrichment for the overlapping genes identified in (C).

(G) Schema illustrates that persistent expression of genes of the Wnt signal pathway causes the failure of the transition from NPs to RGPs and ultimately the disruption of the cortical architecture.

addition of Wnt pathway activators. This unique structure might be spontaneously generated by the cells to maintain their self-proliferative state. Additionally, the mechanism behind the formation of this structure does not seem to depend solely on Wnt pathway activation, suggesting other regulatory mechanisms might be involved. To further elucidate the formation mechanism of this rosette structure, future research could use *in vitro* organoid systems for more in-depth exploration. This will help achieve a more comprehensive understanding of the self-organization and proliferation processes of neural stem cells.

STAR★METHODS

Detailed methods are provided in the online version of this paper and include the following:

- KEY RESOURCES TABLE
- RESOURCE AVAILABILITY
  - Lead contact
  - Materials availability
  - Data and code availability
- EXPERIMENTAL MODEL AND STUDY PARTICIPANT DETAILS
  - Experimental animals
- METHOD DETAILS
  - Immunohistochemistry
  - Quantitative real-time PCR (q-PCR)
  - In utero electroporation (IUE)
  - RNA-seq and data analysis
  - Single-cell RNA-seq and analysis
  - CUT&Tag and data analysis
  - Wnt inhibitor injection
- QUANTIFICATION AND STATISTICAL ANALYSIS

SUPPLEMENTAL INFORMATION

Supplemental information can be found online at https://doi.org/10.1016/j.isci.2024.110600.

ACKNOWLEDGMENTS

We thank members of the Xie laboratory for helpful discussions. We are grateful to Prof. Seiser (Medical University of Vienna) and Prof. Matthias (University of Basel) for generously providing HDAC1$^{f/f}$ and HDAC2$^{f/f}$ mice. We thank the core facility of IOBS for their expertise in microscopy. This study was supported by STI2030-Major Projects 2021ZD0202304, the National Natural Science Foundation of China (32271020 to Y.X. and 32100786 to T.T.), the Program of Shanghai Academic Research Leader (22XD1400400) the ZJ Lab and Shanghai Center for Brain Science and Brain-Inspired Technology to Y.X.

AUTHOR CONTRIBUTIONS

Y.X. conceived and designed the project. Z.Y. designed and performed bioinformatic analysis. Y.H. performed experiments with help from T.T., Z.Y., and Y.X. wrote the manuscript with input from other authors. Y.X. supervised the project.

DECLARATION OF INTERESTS

The authors declare no competing interest.

Received: April 8, 2024
Revised: June 19, 2024
Accepted: July 24, 2024
Published: July 27, 2024

REFERENCES

1. Götz, M., and Huttner, W.B. (2005). The cell biology of neurogenesis. Nat. Rev. Mol. Cell Biol. *6*, 777–788. https://doi.org/10.1038/nrm1739.
2. Taverna, E., Götz, M., and Huttner, W.B. (2014). The Cell Biology of Neurogenesis: Toward an Understanding of the Development and Evolution of the Neocortex. Annu. Rev. Cell Dev. Biol. *30*, 465–502. https://doi.org/10.1146/annurev-cellbio-101011-155801.
3. Kriegstein, A., and Alvarez-Buylla, A. (2009). The Glial Nature of Embryonic and Adult Neural Stem Cells. Annu. Rev. Neurosci. *32*, 149–184. https://doi.org/10.1146/annurev.neuro.051508.135600.
4. Homem, C.C.F., Repic, M., and Knoblich, J.A. (2015). Proliferation control in neural stem and progenitor cells. Nat. Rev. Neurosci. *16*, 647–659. https://doi.org/10.1038/nrn4021.
5. Koo, B., Lee, K.-H., Ming, G.L., Yoon, K.-J., and Song, H. (2023). Setting the clock of neural progenitor cells during mammalian corticogenesis. Semin. Cell Dev. Biol. *142*, 43–53. https://doi.org/10.1016/j.semcdb.2022.05.013.
6. Sahara, S., and O'Leary, D.D.M. (2009). Fgf10 Regulates Transition Period of Cortical Stem Cell Differentiation to Radial Glia Controlling Generation of Neurons and Basal Progenitors. Neuron *63*, 48–62. https://doi.org/10.1016/j.neuron.2009.06.006.
7. Zeng, B., Liu, Z., Lu, Y., Zhong, S., Qin, S., Huang, L., Zeng, Y., Li, Z., Dong, H., Shi, Y., et al. (2023). The single-cell and spatial transcriptional landscape of human gastrulation and early brain development. Cell Stem Cell *30*, 851–866.e7. https://doi.org/10.1016/j.stem.2023.04.016.
8. Ruan, X., Kang, B., Qi, C., Lin, W., Wang, J., and Zhang, X. (2021). Progenitor cell diversity in the developing mouse neocortex. Proc. Natl. Acad. Sci. USA *118*, e2018866118. https://doi.org/10.1073/pnas.2018866118.
9. Benito-Kwiecinski, S., Giandomenico, S.L., Sutcliffe, M., Riis, E.S., Freire-Pritchett, P., Kelava, I., Wunderlich, S., Martin, U., Wray, G.A., McDole, K., and Lancaster, M.A. (2021). An early cell shape transition drives evolutionary expansion of the human forebrain. Cell *184*, 2084–2102.e19. https://doi.org/10.1016/j.cell.2021.02.050.
10. Nowakowski, T.J., Pollen, A.A., Sandoval-Espinosa, C., and Kriegstein, A.R. (2016). Transformation of the Radial Glia Scaffold Demarcates Two Stages of Human Cerebral Cortex Development. Neuron *91*, 1219–1227. https://doi.org/10.1016/j.neuron.2016.09.005.
11. Liu, J., and Silver, D.L. (2021). Founder cells shape brain evolution. Cell *184*, 1965–1967. https://doi.org/10.1016/j.cell.2021.03.045.
12. Tang, T., Zhang, Y., Wang, Y., Cai, Z., Lu, Z., Li, L., Huang, R., Hagelkruys, A., Matthias, P., Zhang, H., et al. (2019). HDAC1 and HDAC2 Regulate Intermediate Progenitor Positioning to Safeguard Neocortical Development. Neuron *101*, 1117–1133.e5. https://doi.org/10.1016/j.neuron.2019.01.007.
13. Kelly, R.D.W., and Cowley, S.M. (2013). The physiological roles of histone deacetylase (HDAC) 1 and 2: complex co-stars with multiple leading parts. Biochem. Soc. Trans. *41*, 741–749. https://doi.org/10.1042/BST20130010.
14. Montgomery, R.L., Davis, C.A., Potthoff, M.J., Haberland, M., Fielitz, J., Qi, X., Hill, J.A., Richardson, J.A., and Olson, E.N. (2007). Histone deacetylases 1 and 2 redundantly regulate cardiac morphogenesis, growth, and contractility. Genes Dev. *21*, 1790–1802. https://doi.org/10.1101/gad.1563807.
15. Langfelder, P., and Horvath, S. (2008). WGCNA: an R package for weighted correlation network analysis. BMC Bioinf. *9*, 559. https://doi.org/10.1186/1471-2105-9-559.
16. Chenn, A., and Walsh, C.A. (2002). Regulation of cerebral cortical size by control of cell cycle exit in neural precursors. Science *297*, 365–369. https://doi.org/10.1126/science.1074192.
17. Foroutan, M., Bhuva, D.D., Lyu, R., Horan, K., Cursons, J., and Davis, M.J. (2018). Single sample scoring of molecular phenotypes. BMC Bioinf. *19*, 404. https://doi.org/10.1186/s12859-018-2435-4.
18. Chen, B., Khodadoust, M.S., Liu, C.L., Newman, A.M., and Alizadeh, A.A. (2018). Profiling tumor infiltrating immune cells with CIBERSORT. Methods Mol. Biol. *1711*, 243–259. https://doi.org/10.1007/978-1-4939-7493-1_12.
19. Di Bella, D.J., Habibi, E., Stickels, R.R., Scalia, G., Brown, J., Yadollahpour, P., Yang, S.M., Abbate, C., Biancalani, T., Macosko, E.Z., et al. (2021). Molecular logic of cellular diversification in the mouse cerebral cortex. Nature *595*, 554–559. https://doi.org/10.1038/s41586-021-03670-5.
20. Jin, S., Guerrero-Juarez, C.F., Zhang, L., Chang, I., Ramos, R., Kuan, C.-H., Myung, P., Plikus, M.V., and Nie, Q. (2021). Inference and analysis of cell-cell communication using CellChat. Nat. Commun. *12*, 1088. https://doi.org/10.1038/s41467-021-21246-9.
21. Haberland, M., Montgomery, R.L., and Olson, E.N. (2009). The many roles of histone deacetylases in development and physiology: implications for disease and therapy. Nat. Rev. Genet. *10*, 32–42. https://doi.org/10.1038/nrg2485.
22. Kaya-Okur, H.S., Janssens, D.H., Henikoff, J.G., Ahmad, K., and Henikoff, S. (2020). Efficient low-cost chromatin profiling with CUT&Tag. Nat. Protoc. *15*, 3264–3283.
23. Heinz, S., Benner, C., Spann, N., Bertolino, E., Lin, Y.C., Laslo, P., Cheng, J.X., Murre, C., Singh, H., and Glass, C.K. (2010). Simple combinations of lineage-determining transcription factors prime cis-regulatory elements required for macrophage and B cell identities. Mol. Cell *38*, 576–589. https://doi.org/10.1016/j.molcel.2010.05.004.
24. Fardi, M., Alivand, M., Baradaran, B., Farshdousti Hagh, M., and Solali, S. (2019). The crucial role of ZEB2: From development to epithelial-to-mesenchymal transition and cancer complexity. J. Cell. Physiol. *234*, 14783–14799. https://doi.org/10.1002/jcp.28277.
25. Price, J.D., Lindtner, S., Ypsilanti, A., Binyameen, F., Johnson, J.R., Newton, B.W., Krogan, N.J., and Rubenstein, J.L.R. (2022). DLX1 and the NuRD complex cooperate in enhancer decommissioning and transcriptional repression. Development *149*, dev199508. https://doi.org/10.1242/dev.199508.
26. Huang, S.-M.A., Mishina, Y.M., Liu, S., Cheung, A., Stegmeier, F., Michaud, G.A., Charlat, O., Wiellette, E., Zhang, Y., Wiessner, S., et al. (2009). Tankyrase inhibition stabilizes axin and antagonizes Wnt signalling. Nature *461*, 614–620. https://doi.org/10.1038/nature08356.
27. Bystron, I., Blakemore, C., and Rakic, P. (2008). Development of the human cerebral cortex: Boulder Committee revisited. Nat. Rev. Neurosci. *9*, 110–122. https://doi.org/10.1038/nrn2252.
28. Aaku-Saraste, E., Hellwig, A., and Huttner, W.B. (1996). Loss of Occludin and Functional Tight Junctions, but Not ZO-1, during Neural Tube Closure—Remodeling of the Neuroepithelium Prior to Neurogenesis. Dev. Biol. *180*, 664–679. https://doi.org/10.1006/dbio.1996.0336.
29. Lui, J.H., Hansen, D.V., and Kriegstein, A.R. (2011). Development and evolution of the human neocortex. Cell *146*, 18–36. https://doi.org/10.1016/j.cell.2011.06.030.
30. Wippold, F.J., and Perry, A. (2006). Neuropathology for the Neuroradiologist: Rosettes and Pseudorosettes. AJNR. Am. J. Neuroradiol. *27*, 488–492.
31. Cotter, J.A., and Judkins, A.R. (2022). Evaluation and Diagnosis of Central Nervous System Embryonal Tumors (Non-Medulloblastoma). Pediatr. Dev. Pathol. *25*, 34–45. https://doi.org/10.1177/10935266211018554.
32. Backman, M., Machon, O., Mygland, L., van den Bout, C.J., Zhong, W., Taketo, M.M., and Krauss, S. (2005). Effects of canonical Wnt signaling on dorso-ventral specification of the mouse telencephalon. Dev. Biol. *279*, 155–168. https://doi.org/10.1016/j.ydbio.2004.12.010.
33. Winter, M., Moser, M.A., Meunier, D., Fischer, C., Machat, G., Mattes, K., Lichtenberger, B.M., Brunmeir, R., Weissmann, S., Murko, C., et al. (2013). Divergent roles of HDAC1 and HDAC2 in the regulation of epidermal development and tumorigenesis: HDAC1 negatively controls epidermal proliferation. EMBO J. *32*, 3176–3191. https://doi.org/10.1038/emboj.2013.243.
34. Gorski, J.A., Talley, T., Qiu, M., Puelles, L., Rubenstein, J.L.R., and Jones, K.R. (2002). Cortical Excitatory Neurons and Glia, But Not GABAergic Neurons, Are Produced in the Emx1-Expressing Lineage. J. Neurosci. *22*, 6309–6314. https://doi.org/10.1523/JNEUROSCI.22-15-06309.2002.
35. Hao, Y., Hao, S., Andersen-Nissen, E., Mauck, W.M., Zheng, S., Butler, A., Lee, M.J., Wilk, A.J., Darby, C., Zager, M., et al. (2021). Integrated analysis of multimodal single-cell data. Cell *184*, 3573–3587.e29. https://doi.org/10.1016/j.cell.2021.04.048.
36. Kim, D., Paggi, J.M., Park, C., Bennett, C., and Salzberg, S.L. (2019). Graph-based genome alignment and genotyping with HISAT2 and HISAT-genotype. Nat. Biotechnol. *37*, 907–915. https://doi.org/10.1038/s41587-019-0201-4.
37. Langmead, B., and Salzberg, S.L. (2012). Fast gapped-read alignment with Bowtie 2. Nat. Methods *9*, 357–359. https://doi.org/10.1038/nmeth.1923.
38. Xie, Y., Jüschke, C., Esk, C., Hirotsune, S., and Knoblich, J.A. (2013). The Phosphatase PP4c Controls Spindle Orientation to Maintain Proliferative Symmetric Divisions in the Developing Neocortex. Neuron *79*, 254–265. https://doi.org/10.1016/j.neuron.2013.05.027.

39. Liao, Y., Smyth, G.K., and Shi, W. (2014). featureCounts: an efficient general purpose program for assigning sequence reads to genomic features. Bioinformatics *30*, 923–930. https://doi.org/10.1093/bioinformatics/btt656.
40. Love, M.I., Huber, W., and Anders, S. (2014). Moderated estimation of fold change and dispersion for RNA-seq data with DESeq2. Genome Biol. *15*, 550. https://doi.org/10.1186/s13059-014-0550-8.
41. Wu, T., Hu, E., Xu, S., Chen, M., Guo, P., Dai, Z., Feng, T., Zhou, L., Tang, W., Zhan, L., et al. (2021). clusterProfiler 4.0: A universal enrichment tool for interpreting omics data. Innovation *2*, 100141. https://doi.org/10.1016/j.xinn.2021.100141.
42. Ramírez, F., Dündar, F., Diehl, S., Grüning, B.A., and Manke, T. (2014). deepTools: a flexible platform for exploring deep-sequencing data. Nucleic Acids Res. *42*, W187–W191. https://doi.org/10.1093/nar/gku365.
43. Zheng, G.X.Y., Terry, J.M., Belgrader, P., Ryvkin, P., Bent, Z.W., Wilson, R., Ziraldo, S.B., Wheeler, T.D., McDermott, G.P., Zhu, J., et al. (2017). Massively parallel digital transcriptional profiling of single cells. Nat. Commun. *8*, 14049. https://doi.org/10.1038/ncomms14049.
44. Fleming, S.J., Chaffin, M.D., Arduini, A., Akkad, A.-D., Banks, E., Marioni, J.C., Philippakis, A.A., Ellinor, P.T., and Babadi, M. (2023). Unsupervised removal of systematic background noise from droplet-based single-cell experiments using CellBender. Nat. Methods *20*, 1323–1335. https://doi.org/10.1038/s41592-023-01943-7.
45. Quinlan, A.R., and Hall, I.M. (2010). BEDTools: a flexible suite of utilities for comparing genomic features. Bioinformatics *26*, 841–842. https://doi.org/10.1093/bioinformatics/btq033.
46. Meers, M.P., Tenenbaum, D., and Henikoff, S. (2019). Peak calling by Sparse Enrichment Analysis for CUT&RUN chromatin profiling. Epigenet. Chromatin *12*, 42. https://doi.org/10.1186/s13072-019-0287-4.
47. Stark, R., and Brown, G. DiffBind: Differential binding analysis of ChIP-Seq peak data. (R package version 3.2.7). https://bioconductor.org/packages/release/bioc/html/DiffBind.html.
48. Yu, G., Wang, L.-G., and He, Q.-Y. (2015). ChIPseeker: an R/Bioconductor package for ChIP peak annotation, comparison and visualization. Bioinformatics *31*, 2382–2383. https://doi.org/10.1093/bioinformatics/btv145.

STAR★METHODS

KEY RESOURCES TABLE

REAGENT or RESOURCE	SOURCE	IDENTIFIER
Antibodies		
Rabbit anti-Arl13b	Proteintech	Cat#17711-1-AP; RRID:AB_2060867
Chicken anti-GFP	Abcam	Cat#ab13970; RRID:AB_300798
Chicken anti-GFP	Aves Labs	Cat#GFP-1020; RRID:AB_10000240
Rabbit anti-Hdac1	Abcam	Cat#ab7028; RRID:AB_305705
Rabbit anti-Hdac2	HuaAn Biotechnoloy	Cat#ET1607-78; RRID:AB_2756440
Mouse anti-N-Cadherin	BD	Cat#610920; RRID:AB_2077527
Rabbit anti-Pax6	MBL International	Cat#PD022; RRID:AB_1520876
Rabbbit anti-Sox2	Abcam	Cat#ab97959; RRID:AB_2341193
Mouse anti-Tuj1	Abcam	Cat#ab7751; RRID:AB_306045
Mouse-ZO-1	Thermo Fisher Scientific	Cat#33–9100, RRID:AB_2533147
Donkey anti-Rabbit IgG (H + L) Highly Cross-Adsorbed Secondary Antibody, Alexa Fluor 488	Invitrogen	Cat#A21206; RRID: AB_2535792
Goat anti-Rabbit IgG (H + L) Highly Cross-Adsorbed Secondary Antibody, Alexa Fluor 568	Invitrogen	Cat#A11036; RRID: AB_10563566
Donkey anti-Mouse IgG (H + L) Highly Cross-Adsorbed Secondary Antibody, Alexa Fluor 568	Invitrogen	Cat#A10037; RRID: AB_2534013
Alexa Fluor 488 AffiniPure Donkey Anti-Chicken IgY (IgG) (H + L) antibody	Jackson ImmunoResearch	Cat#703-545-155; RRID: AB_2340375
Alexa Fluor 647 AffiniPure Donkey Anti-Mouse IgG (H + L) antibody	Jackson ImmunoResearch	Cat#715-605-151; RRID: AB_2340863
Donkey anti-Goat IgG (H + L) Cross-Adsorbed Secondary Antibody, Alexa Fluor 568	Invitrogen	Cat#A11057; RRID: AB_2534104
Chemicals, peptides, and recombinant proteins		
DAPI	Sigma Corporation of America	Cat#D9542
DMSO	Sigma	Cat#V900090
XAV-939	Tocris Bioscience	Cat#3748
Pierce™ Protease and Phosphatase Inhibitor Mini Tablets, EDTA Free	Thermo Fisher Scientific	Cat#A32955
Trizol	Thermo Fisher Scientific	Cat#15596026CN
Papain	Worthington	Cat#LK003178
VAHTS DNA Clean Beads	Vazyme	Cat#N411-01
Critical commercial assays		
Equalbit® 1 × dsDNA HS Assay Kit	Vazyme	Cat#EQ121-02
Hyperactive *In-Situ* ChIP Library Prep Kit for Illumina	Vazyme	Cat#TD901
TruePrep Index Kit V2 for Illumina	Vazyme	Cat#TD202
Deposited data		
Raw and analyzed RNA-seq data	This paper	GEO: GSE251727
Raw and analyzed scRNA-seq data	This paper	GEO: GSE2517277
Raw and analyzed H3K27ac CUT&Tag data	This paper	GEO: GSE2517277
scRNA-seq data of mouse cortical	Ruan et al.[8]	GEO: GSE161690
scRNA-seq data of mouse cortical	Di Bella et al.[19]	GEO: GSE153164
HDAC1/2 ChIPseq data	Price et al.[25]	GEO: GSE194076

(*Continued on next page*)

Continued

REAGENT or RESOURCE	SOURCE	IDENTIFIER
Experimental models: Organisms/strains		
Mouse: Hdac1$^{f/f}$; Hdac2$^{f/f}$	Winter et al., 2013[33]	N/A
Mouse: Emx1-Cre/Cre	Gorski et al., 2002[34]	N/A
Oligonucleotides		
GAPDH q-PCR primers forward: CCACTCACGGCAAATTCAAC reverse: CTCCACGACATACTCAGCAC	This study	N/A
Hmga2 q-PCR primers forward: AGTTTGGAGAACGCACCAGG reverse: GGATGTCTCTTCAGTCTCCCATGA	This study	N/A
Occludin q-PCR primers forward: GAGTGAAGAGTACATGGCTGC reverse: CTTCTCCCGCAACTGGCATC	This study	N/A
Cldn6 q-PCR primers forward: ACCTGGAAATCTTAGCAGTCT reverse: CTGTTGCCGATGAAGGCG	This study	N/A
Epcam q-PCR primers forward: CGTTGATGAAAAGGCACCCG reverse: CCCATCTCCTTTATCTCAGCCT	This study	N/A
CDH1 q-PCR primers forward: CGCCACAGATGATGGTTCAC reverse: GCAGTAAAGGGGGACGTGTT	This study	N/A
CDH2 q-PCR primers forward: CTTCTCAATGTGAAATTCAGC reverse: TGGTTCCTTCATAGGCTCCT	This study	N/A
Wnt5b clone primers forward: CTTTGGAAGATGTTGGTCCC reverse: CTTACAGACATACTGGTCCA	This study	N/A
Wnt9a clone primers forward: CCCGGAGCGCGATGGTCTG reverse: GCCCTTGCAGGTATAGACCTC	This study	N/A
Recombinant DNA		
p3xFLAG-CMV-14-Wnt5b	This study	N/A
p3xFLAG-CMV-14-Wnt9a	This study	N/A
Software and algorithms		
NIS Element version 5.11	Nikon	https://www.microscope.healthcare.nikon.com/products/software;
GraphPad Prism	GraphPad Software	https://www.graphpad.com/scientific-software/prism/;
Adobe Photoshop	Adobe	https://www.adobe.com/products/photoshop.html
Adobe Illustrator	Adobe	http://www.adobe.com/products/illustrator.html
R v4.1.3	N/A	http://www.r-project.org
Seurat v4.3.0	Hao et al.[35]	https://github.com/satijalab/seurat/releases/tag/v4.3.0
Cell Ranger v.7.1.0	10x Genomics	https://support.10xgenomics.com/single-cell-gene-expression/software/overview/welcome
HISAT2 v2.2.1	Kim et al., 2019[36]	http://daehwankimlab.github.io/hisat2/

(*Continued on next page*)

Continued

REAGENT or RESOURCE	SOURCE	IDENTIFIER
ggplot2 v3.3.6	R package	https://ggplot2.tidyverse.org/
Bowtie2 v2.2.5	Langmead and Salzberg[37]	https://github.com/BenLangmead/bowtie2
Python 3.8.16	N/A	https://www.python.org/downloads/release/python-3816/
ImageJ	NIH	https://imagej.nih.gov/ij/

RESOURCE AVAILABILITY

Lead contact

Further information and requests for resources and reagents should be directed to and will be fulfilled by the Lead Contact Yunli Xie (yunli.xie@fudan.edu.cn).

Materials availability

This study did not generate new unique reagents.

Data and code availability

- The scRNA-seq, RNA-seq and H3K27ac CUT&Tag data have been deposited at GEO and are publicly available as of the date of publication. Accession numbers are listed in the key resources table. This paper analyzes existing scRNA-seq and HDAC1/2 ChIPseq, publicly available data. These accession numbers for the datasets are listed in the key resources table.
- This paper does not report original code.
- Any additional information required to reanalyze the data reported in this paper is available from the lead contact upon request.

EXPERIMENTAL MODEL AND STUDY PARTICIPANT DETAILS

Experimental animals

Mice with homozygous HDAC1$^{f/f}$ and HDAC2$^{f/f}$ genotypes[33] were bred with Emx1-Cre mice[34] to produce HDAC1$^{f/+}$; HDAC2$^{f/+}$; Emx1-Cre progeny. These progenies were then bred with HDAC1$^{f/f}$;HDAC2$^{f/f}$ mice, successfully creating double conditional knockout (HDAC1/2 cKO) mice. All experimental subjects, both male and female, were randomly allocated to different groups. For the experiments, we utilized embryos from stages E9.5 to E16.5, collected through timed pregnancies. All our mouse experiments received approval from the Ethics Committee of Shanghai Medical College, Fudan University, under approval number 2018IOBSJS-005.

METHOD DETAILS

Immunohistochemistry

Post-dissection, we fixed the embryonic brains overnight in 4% paraformaldehyde (PFA) at 4°C. They were then dehydrated in 30% sucrose in PBS until fully submerged. Next, the brains were embedded in O.C.T compound (Sakura) and sectioned at 14μm using a Leica cryostat (CM1950). The sections were permeabilized with 0.5% Triton X-100, followed by blocking in a buffer (5% donkey serum, 0.05% Triton X-100 in PBS) for an hour at room temperature. Subsequently, they were incubated overnight at 4°C with primary antibodies, then washed thrice in PBS for 5 min. The sections were then incubated for 2 h with fluorescence-conjugated secondary antibodies at room temperature in the dark before mounting. We used primary antibodies including chicken-GFP (1:1000; Abcam, ab13970), chicken-GFP (1:1000; Aves Labs, GFP-1020), rabbit-Arl13b (1:500; Proteintech, 17711-1-AP), rabbit-Pax6(1:800; MBL International, PD022), mouse-ZO-1(1:300; Life Technologies, 33–9100), mouse-N-Cadherin (1:1000; BD, 610920), mouse-Tuj1(1:1000, Sigma-Aldrich, T8660). For secondary antibodies, we used Cy2, Cy3, Cy5 (Jackson ImmunoResearch) or Alexa Fluor 488, 555, 647 (Invitrogen) at 1:500 dilutions.

Quantitative real-time PCR (q-PCR)

The neocortex were isolated from both wild-type (WT) and HDAC1/2 conditional knockout (cKO) embryos. Total RNA extraction utilized TRIzol reagent (ThermoScientific), followed by cDNA synthesis using the SuperScrip III First-Strand Synthesis System (Invitrogen). Real-time PCR was conducted on the QuantStudio 3 Real-Time PCR System (Thermo Fisher Scientific). Quantification was achieved using the QuantStudio Design & Analysis Software (Thermo Fisher Scientific), with data normalized to GAPDH mRNA levels.

In utero electroporation (IUE)

In line with the protocol from Xie et al.,[38] we anesthetized pregnant mice at the appropriate gestational phase and exposed their uterine horns. Plasmids (1.5 mg/mL) were directly injected into the lateral ventricles of the embryos. We used the BTX ECM830 system for

electroporation, delivering five 50 ms pulses at a voltage of 30-32V, depending on the embryonic stage, with 950 ms intervals. After electroporation, we repositioned the uterine horns and carefully sutured the surgical site. The embryonic brains were harvested 1 or 3 days later for further analysis.

RNA-seq and data analysis

Total RNA was isolated from cerebral cortices at E13.5, E14.5, E15.5 and E16.5 using TRIzol reagent (ThermoScientific) according to the manufacturer's instructions. RNA-seq was performed at Novogene Biotech Co., Ltd in Beijing, China.

For data analysis, raw data were first trimmed using Trim Galore v.0.6.7 (https://github.com/FelixKrueger/TrimGalore) then mapped to the mm10 genome by HISAT2[36] v2.2.1 with default parameters. The number of reads mapping to each gene was counted by featureCounts[39] v2.0.1 with parameters: -a gencode.vM20.annotation.gtf. And transcripts per million (TPM) were calculated.

Differential analysis of count data was conducted using DESeq2.[40] Differentially expressed genes were defined as adjusted P-value <0.05 and Foldchange >1.414. Gene Ontology term enrichment analysis was performed using ClusterProfiler[41] v4.2.0. Normalized bigwig files were generated by BamCoverage from Deeptools[42] v3.5.1. WGCNA[15] v1.71 was used to perform the weighted correlation network analysis. PickSoftThreshold function was used to get the best soft-thresholding power 10, with parameters (networkType = 'signed', verbose = 5). Then we constructed network using parameters (networkType = 'signed,' minModuleSize = 30, reassignThreshold = 0, mergeCutHeight = 0.25). The data was dissected into 10 modules and the module eigengenes were used for downstream analysis.

Single-cell RNA-seq and analysis

Single-cell library preparation and sequencing

Single cells isolated from the cerebral cortices of both wild-type (WT) and HDAC1/2 conditional knockout (cKO) mice at embryonic day 12.5 (E12.5) were processed using the Chromium 10x system for single-cell cDNA generation. The libraries were then prepared to employ the Chromium Single Cell 3' GEM, Library & Gel Bead Kit v3, strictly adhering to the manufacturer's instructions. Following the cDNA clean-up, the libraries were quantified using a BioAnalyzer then were sequenced on the Illumina NovaSeq 6000.

Library pre-processing

Raw sequencing data (fastq files) were aligned to the reference genome mm10 (cellranger ref. 2020-A, and Ensembl v98 gene annotation) using the Cell Ranger[43] pipeline (v.7.1.0, 10x Genomics) with parameters: –include-introns = false –r2-length = 91 –r1-length = 28. After alignment, filtering, barcode counting, and UMI counting we use feature-barcode matrices for downstream analysis. We evaluated the ambient RNA contamination in each sample utilizing CellBender[44] (v0.2.0), employing the 'remove-background' function with default parameters. Subsequent comparative analysis of count data, pre- and post-correction, revealed minimal discrepancies (data not shown). Based on this observation, we proceeded with the downstream analysis without implementing any adjustments for ambient RNA contamination.

Cell filtering

We used Seurat[35] (v4.3.0) within R (v4.1.3) for analysis. Our rigorous quality control excluded cells with UMI counts over 7,500 or under 500, and those with mitochondrial gene counts above 20%, hemoglobin gene counts over 25%, or ribosomal gene counts exceeding 50%. We then merged the HDAC1/2 cKO and control samples using Seurat's merge function. This process resulted in a data matrix encompassing 32,285 genes across 29,281 cells.

Normalization and cell clustering

The count matrix underwent normalization relative to library size, followed by logarithmic transformation and scaling, in line with the standard workflow detailed in the Seurat tutorial (https://satijalab.org/seurat/), using default parameters except where specified otherwise. For the normalization of UMI count data, regularized negative binomial regression was employed, facilitated through the Seurat function SCTransform. In Seurat, principal component analysis was conducted for dimensionality reduction, focusing on the 3000 genes with the most significant expression variability across cells. We constructed a shared nearest neighbor graph, basing it on the Euclidean distance within the first 15 identified principal components, and applied the Louvain algorithm for cluster detection. Initial clustering, set at a default resolution of 0.3, yielded 11 distinct clusters. The cortical Emx1-lineage cells were classified as the collective of NPC1, NPC2, IPC, and Neuron. We further proceeded to subset and re-cluster the Emx1-lineage cells, concentrating on the 3000 most variable genes and the initial 15 principal components.

Visualization and differential expression analysis

In our study, data visualization was conducted using the Uniform Manifold Approximation and Projection (UMAP) technique, as demonstrated in Figure 3A. For the analysis of differential gene expression, the FindAllMarkers function from the Seurat package was employed, using the default settings. The selection of final marker genes was based on criteria that included Wilcoxon Rank-Sum test p values (less than 0.05) and an average log fold change exceeding 0.25.

Cell-cell communication analysis

In our analysis, the CellChat[20] package v1.6.1, was employed to examine cell-cell interactions among different cell types within single-cell RNA sequencing data. While default settings were primarily used, there were specific deviations: the algorithm was set to perform 10,000 permutations, and interactions were only considered significant if a cell type group was represented by 10 or more cells. To evaluate the predominant signaling pathways within these cell subsets, we utilized the 'CellChatDB.mouse' database. Additionally, the functions 'netVisual_aggregate' and 'netVisual_individual' were applied to assess the intensity of the cell–cell communication networks. It's important to note that the analyses for wild-type (WT) and HDAC1/2 cKO samples were conducted separately.

CUT&Tag and data analysis

Histone modifications in this study were identified using the Cleavage Under Targets and Tagmentation (CUT&Tag) technique, following the protocol published by the Henikoff lab. For both wild-type (WT) and HDAC1/2 conditional knockout (cKO) cerebral cortices, three biological replicates were prepared. We employed the Rabbit anti-H3K27ac antibody (Abcam Ab4729) for specific targeting. The Tn5-tagmented DNA fragments were then amplified using the 2x CAM Mix, a uniquely barcoded i5 primer, and a uniquely barcoded i7 primer, undergoing 12 amplification cycles. Libraries were quantified on a Qubit 4 fluorometer (Thermo Fisher Scientific Q33226). We performed size selection on the libraries, isolating DNA fragments exceeding 300 base pairs using VAHTS DNA Clean Beads (Vazyme N411).

We used the Henikoff lab published CUT&Tag Data Analysis pipeline for data analysis. Raw data were aligned to the GRCm38/mm10 genome by Bowtie2 v2.2.5 using parameters: -end-to-end –very-sensitive –no-mixed –no-discordant –phred33 -I 10 -X 700. Bam files were converted to paired-end BED files using BEDTools v2.30.0 bamtobed with the -bedpe flag, then the read pairs that are on the same chromosome and fragment length less than 1000bp were selected to generate a new BED file, and finally we converted bed file to a bedgraph file using genomecov from BEDTools.[45] Peaks were called using SEACR[46] v.1.3.0 with the parameters: −0.01 -norm -stringent. Normalized bigwig files were generated by BamCoverage from Deeptools v3.5.1, which were then visualized on IGV v2.16.2. Diffbind[47] v3.2.7 was used for differential peaks binding affinity analysis. First, the consensus peak binding affinity matrix was calculated by Diffbind: dba.count (bUseSummarizeOverlaps = TRUE, summits = FALSE). Then, the differential peaks were calculated by DESeq2, and annotatePeak function from ChIPseeker[48] v1.30.0 was used for peak annotation (getPromoters: upstream = 1000, downstream = 1000). Motif search was carried out with HOMER v.4.11.0 "findmotifs.pl" function.

Wnt inhibitor injection

XAV-939 (Tocris Bioscience, Cat. No.3748) was dissolved in the vehicle (DMSO). Pregnant mice at embryonic 12.5 were subjected to anesthesia, followed by the exposure of the uterine horns. Vehicle (1 μL) or XAV-939 (1 μL of a 0.5 mg/mL solution) was injected into the lateral ventricle of embryos. 3 days later, the embryonic brains were collected for further analysis.

QUANTIFICATION AND STATISTICAL ANALYSIS

Data analysis and plot generation were conducted using R software and GraphPad Prism software. Detailed statistical analyses are described in the figure legends. For comparisons between two groups, a two-tailed Student's t test was utilized, assuming normal data distribution. Due to the distinct phenotype in mutants, data collection and analysis were not blinded to the experimental conditions. RT-qPCR data were normalized to the mean expression of the housekeeping gene GAPDH and analyzed using the 2-ΔΔCt method to compare relative gene expression levels. Data are presented as mean ± SEM. Statistical significance was defined as $p < 0.05$. Significance levels are indicated as *$p < 0.05$; **$p < 0.01$; and ***$p < 0.001$.